



Depth-resolved local reflectance spectra measurements in full-field optical coherence tomography

RÉMY CLAVEAU,^{1,2,*} PAUL MONTGOMERY,¹ MANUEL FLURY,^{1,2} AND DENIS MONTANER¹

¹Laboratoire des Sciences de l'Ingénieur, de l'Informatique et de l'Imagerie (ICube), UDS-CNRS UMR 7357, 23 Rue du Læss, 67037 Strasbourg, France

²Institut National des Sciences Appliquées de Strasbourg (INSA Strasbourg), 24 Boulevard de la Victoire, 67084 Strasbourg cedex, France

*r.claveau@unistra.fr

Abstract: Full-field optical coherence tomography (FF-OCT) is a widely used technique for applications such as biological imaging, optical metrology, and materials characterization, providing structural and spectral information. By spectral analysis of the backscattered light, the technique of spectroscopic-OCT enables the differentiation of structures having different spectral properties, but not the determination of their reflectance spectrum. For surface measurements, this can be achieved by applying a Fourier transform to the interferometric signals and using an accurate calibration of the optical system. An extension of this method is reported for local spectroscopic characterization of transparent samples and in particular for the determination of depth-resolved reflectance spectra of buried interfaces. The correct functioning of the method is demonstrated by comparing the results with those obtained using a program based on electromagnetic matrix methods for stratified media. Experimental measurements of spatial resolutions are provided to demonstrate the smallest structures that can be characterized.

© 2017 Optical Society of America

OCIS codes: (180.1655) Coherence tomography; (120.3180) Interferometry; (120.2650) Fringe analysis; (300.6300) Spectroscopy, Fourier transforms.

References and links

1. U. Morgner, W. Drexler, F. X. Kärtner, X. D. Li, C. Pitris, E. P. Ippen, and J. G. Fujimoto, "Spectroscopic optical coherence tomography," *Opt. Lett.* **25**(2), 111–113 (2000).
2. A. Dubois, J. Moreau, and C. Boccara, "Spectroscopic ultrahigh-resolution full-field optical coherence microscopy," *Opt. Express* **16**(21), 17082–17091 (2008).
3. R. Leitgeb, M. Wojtkowski, A. Kowalczyk, C. K. Hitzenberger, M. Sticker, and A. F. Fercher, "Spectral measurement of absorption by spectroscopic frequency-domain optical coherence tomography," *Opt. Lett.* **25**(11), 820–822 (2000).
4. D. Adler, T. Ko, P. Herz, and J. Fujimoto, "Optical coherence tomography contrast enhancement using spectroscopic analysis with spectral autocorrelation," *Opt. Express* **12**(22), 5487–5501 (2004).
5. D. Vobornik, G. Margaritondo, J. S. Sanghera, P. Thielen, I. D. Aggarwal, B. Ivanov, N. H. Tolk, V. Manni, S. Grimaldi, A. Lisi, S. Rieti, D. W. Piston, R. Generosi, M. Luce, P. Perfetti, and A. Cridenti, "Spectroscopic infrared scanning near-field optical microscopy (IR-SNOM)," *J. Alloys Compd.* **401**(1-2), 80–85 (2005).
6. M. Brehm, T. Taubner, R. Hillenbrand, and F. Keilmann, "Infrared spectroscopic mapping of single nanoparticles and viruses at nanoscale resolution," *Nano Lett.* **6**(7), 1307–1310 (2006).
7. S. Amarie, T. Ganz, and F. Keilmann, "Mid-infrared near-field spectroscopy," *Opt. Express* **17**(24), 21794–21801 (2009).
8. D. T. Dicker, J. Lerner, P. Van Belle, S. F. Barth, D. Guerry 4th, M. Herlyn, D. E. Elder, and W. S. El-Deiry, "Differentiation of normal skin and melanoma using high resolution hyperspectral imaging," *Cancer Biol. Ther.* **5**(8), 1033–1038 (2006).
9. S. J. Leavesley, N. Annamdevula, J. Boni, S. Stocker, K. Grant, B. Troyanovsky, T. C. Rich, and D. F. Alvarez, "Hyperspectral imaging microscopy for identification and quantitative analysis of fluorescently-labeled cells in highly autofluorescent tissue," *J. Biophotonics* **5**(1), 67–84 (2012).
10. K. J. Zuzak, M. D. Schaeberle, E. N. Lewis, and I. W. Levin, "Visible Reflectance Hyperspectral Imaging: Characterization of a Noninvasive, in Vivo System for Determining Tissue Perfusion," *Anal. Chem.* **74**(9), 2021–2028 (2002).

11. T. E. Matthews, M. Medina, J. R. Maher, H. Levinson, W. J. Brown, and A. Wax, "Deep tissue imaging using spectroscopic analysis of multiply scattered light," *Optica* **1**(2), 105 (2014).
12. E. Betzig and J. K. Trautman, "Near-field optics: microscopy, spectroscopy, and surface modification beyond the diffraction limit," *Science* **257**(5067), 189–195 (1992).
13. H. Zhou, A. Midha, G. Mills, L. Donaldson, and J. M. R. Weaver, "Scanning near-field optical spectroscopy and imaging using nanofabricated probes," *Appl. Phys. Lett.* **75**(13), 1824–1826 (1999).
14. F. Huth, A. Govyadinov, S. Amarie, W. Nuansing, F. Keilmann, and R. Hillenbrand, "Nano-FTIR absorption spectroscopy of molecular fingerprints at 20 nm spatial resolution," *Nano Lett.* **12**(8), 3973–3978 (2012).
15. I. Amenabar, S. Poly, W. Nuansing, E. H. Hubrich, A. A. Govyadinov, F. Huth, R. Krutokhvostov, L. Zhang, M. Knez, J. Heberle, A. M. Bittner, and R. Hillenbrand, "Structural analysis and mapping of individual protein complexes by infrared nanospectroscopy," *Nat. Commun.* **4**, 2890 (2013).
16. A. R. Badireddy, M. R. Wiesner, and J. Liu, "Detection, characterization, and abundance of engineered nanoparticles in complex waters by hyperspectral imagery with enhanced Darkfield microscopy," *Environ. Sci. Technol.* **46**(18), 10081–10088 (2012).
17. G. Latour, J. Moreau, M. Elias, and J.-M. Frigerio, "Micro-spectrometry in the visible range with full-field optical coherence tomography for single absorbing layers," *Opt. Commun.* **283**(23), 4810–4815 (2010).
18. R. Claveau, P. C. Montgomery, M. Flury, and D. Montaner, "Local reflectance spectra measurements of surfaces using coherence scanning interferometry," *Proc. SPIE* **9890**, 98900Q (2016).
19. A. Leong-Hoi, R. Claveau, M. Flury, W. Uhring, B. Serio, F. Anstötz, and P. C. Montgomery, "Detection of defects in a transparent polymer with high resolution tomography using white light scanning interferometry and noise reduction," *Proc. SPIE* **9528**, 952807 (2015).
20. D. Y. K. Ko and J. R. Sambles, "Scattering matrix method for propagation of radiation in stratified media: attenuated total reflection studies of liquid crystals," *J. Opt. Soc. Am. A* **5**(11), 1863–1866 (1988).
21. L. A. A. Pettersson, L. S. Roman, and O. Inganäs, "Modeling photocurrent action spectra of photovoltaic devices based on organic thin films," *J. Appl. Phys.* **86**(1), 487–496 (1999).
22. P. C. Montgomery, D. Montaner, and F. Salzenstein, "Tomographic analysis of medium thickness transparent layers using white light scanning interferometry and XZ fringe image processing," *Proc. SPIE* **8430**, 843014 (2012).
23. N. Sultanova, S. Kasarova, and I. Nikolov, "Dispersion proper ties of optical polymers," *Acta Phys. Pol.-. Ser. Gen. Phys.* **116**, 585 (2009).
24. G. Beadie, M. Brindza, R. A. Flynn, A. Rosenberg, and J. S. Shirk, "Refractive index measurements of poly(methyl methacrylate) (PMMA) from 0.4–1.6 μm ," *Appl. Opt.* **54**(31), F139–F143 (2015).
25. G. E. Jellison, Jr., "Optical functions of silicon determined by two-channel polarization modulation ellipsometry," *Opt. Mater.* **1**(1), 41–47 (1992).
26. G. Vuye, S. Fisson, V. N. Van, Y. Wang, J. Rivory, and F. Abeles, "Temperature dependence of the dielectric function of silicon using in situ spectroscopic ellipsometry," *Thin Solid Films* **233**(1-2), 166–170 (1993).
27. S.-W. Kim and G.-H. Kim, "Thickness-profile measurement of transparent thin-film layers by white-light scanning interferometry," *Appl. Opt.* **38**(28), 5968–5973 (1999).
28. T. Jo, K. Kim, S. Kim, and H. Pahk, "Thickness and Surface Measurement of Transparent Thin-Film Layers using White Light Scanning Interferometry Combined with Reflectometry," *J. Opt. Soc. Korea* **18**(3), 236–243 (2014).
29. D. Montaner, P. C. Montgomery, L. Pramatarova, and E. Pecheva, "Analyses locales de couches épaisses complexes par modélisation de la sonde optique en microscopie interférométrique," in *9ème Colloque Francophone Du Club Contrôles et Mesures Optiques Pour l'Industrie (CMOI 2008)*, S. F. d'Optique, ed. (2008).
30. J. F. Biegen, "Calibration requirements for Mirau and Linnik microscope interferometers," *Appl. Opt.* **28**(11), 1972–1974 (1989).
31. F. R. Tolmon and J. G. Wood, "Fringe spacing in interference microscopes," *J. Sci. Instrum.* **33**(6), 236–238 (1956).
32. A. Dubois, J. Selb, L. Vabre, and A.-C. Boccara, "Phase measurements with wide-aperture interferometers," *Appl. Opt.* **39**(14), 2326–2331 (2000).
33. A. Morin and J.-M. Frigerio, "Aperture effect correction in spectroscopic full-field optical coherence tomography," *Appl. Opt.* **51**(16), 3431–3438 (2012).
34. A. Dubois, "Effects of phase change on reflection in phase-measuring interference microscopy," *Appl. Opt.* **43**(7), 1503–1507 (2004).
35. S. Labiau, G. David, S. Gigan, and A. C. Boccara, "Defocus test and defocus correction in full-field optical coherence tomography," *Opt. Lett.* **34**(10), 1576–1578 (2009).
36. A. Federici, H. S. da Costa, J. Ogien, A. K. Ellerbee, and A. Dubois, "Wide-field, full-field optical coherence microscopy for high-axial-resolution phase and amplitude imaging," *Appl. Opt.* **54**(27), 8212–8220 (2015).
37. A. Dubois, K. Grieve, G. Moneron, R. Lecaque, L. Vabre, and C. Boccara, "Ultrahigh-Resolution Full-Field Optical Coherence Tomography," *Appl. Opt.* **43**(14), 2874–2883 (2004).
38. J. G. Fujimoto, C. Pitris, S. A. Boppart, and M. E. Brezinski, "Optical coherence tomography: an emerging technology for biomedical imaging and optical biopsy," *Neoplasia* **2**(1-2), 9–25 (2000).
39. P. C. Montgomery and D. Montaner, "Deep submicron 3D surface metrology for 300 mm wafer characterization using UV coherence microscopy," *Microelectron. Eng.* **45**(2-3), 291–297 (1999).

40. A. Dubois, G. Moneron, and C. Boccara, "Thermal-light full-field optical coherence tomography in the 1.2 μ m wavelength region," *Opt. Commun.* **266**(2), 738–743 (2006).
41. P. Montgomery, D. Benhaddou, and D. Montaner, "Interferometric roughness measurement of Ohmic contact/III–V semiconductor interfaces," *Appl. Phys. Lett.* **71**(13), 1768–1770 (1997).
42. A. Dubois, L. Vabre, A.-C. Boccara, and E. Beaufort, "High-Resolution Full-Field Optical Coherence Tomography with a Linnik Microscope," *Appl. Opt.* **41**(4), 805–812 (2002).
43. M. Born and E. Wolf, *Principles of Optics*, 7th ed. (Cambridge University Press, 1999).
44. J. Kirschner, "On the influence of backscattered electrons on the lateral resolution in scanning auger microscopy," *Appl. Phys. (Berl.)* **14**(4), 351–354 (1977).
45. M. Fauver, E. Seibel, J. R. Rahn, M. Meyer, F. Patten, T. Neumann, and A. Nelson, "Three-dimensional imaging of single isolated cell nuclei using optical projection tomography," *Opt. Express* **13**(11), 4210–4223 (2005).
46. P. D. Woolliams and P. H. Tomlins, "Estimating the resolution of a commercial optical coherence tomography system with limited spatial sampling," *Meas. Sci. Technol.* **22**(6), 065502 (2011).
47. E. Hecht, *Optics* (Addison-Wesley, 2002).
48. I. Zeylikovich, "Short coherence length produced by a spatial incoherent source applied for the Linnik-type interferometer," *Appl. Opt.* **47**(12), 2171–2177 (2008).

1. Introduction

An increasing number of microscopy techniques attempt to combine imaging with spectral characterization, such as with spectroscopic Optical Coherence Tomography (S-OCT) [1–4], spectroscopic infrared scanning near-field optical microscopy (IR-SNOM) [5–7], hyperspectral imaging microscopy [8–10] and still others based on low coherence interferometry (LCI) and spectroscopic analysis of scattered light [11]. With the aim of being able to measure increasingly small structures (biological constituents, nanoparticles...) that can be buried within the depth of a sample, the constraints are that the measurements need to be resolved both spatially and spectrally with a minimal acquisition time. Near field techniques are known for their ability to perform measurements on structures smaller in lateral size than the diffraction limit [12]. Given this, IR-SNOM enables the imaging and spectral determination of structures at a spatial scale of tens of nanometers [13–15]. However, due to the nature of the near-field measurement, to obtain the local spectral information over a large area requires much longer scanning times than far field techniques, and performing depth-resolved measurements is not possible. Recent work on hyperspectral imaging has shown that by coupling this technique with enhanced darkfield microscopy, the imaging, mapping, and characterization of single nanoparticles incorporated in water is possible [16]. Reflectance spectra of nanoparticles extracted from the hyperspectral image cube with a spectral resolution of 1.5 nm has been reported. Due to the system arrangement, nanoparticles with a size smaller than 50 nm can be visualized and measured, as long as they have a low enough density to be distinguished individually, each one having an image size of the Airy spot. In this method, each 2D image (XY image or X λ image) at one given spectral band (or Y position) is obtained independently leading to a sequential recording as a function of the wavelength (or Y position). But, as soon as the spectral band studied is wider or a very fine spectral resolution is desired, the acquisition time also increases. In addition, obtaining quantitative information on the local spectrum of a single structure buried in depth in a transparent sample remains complicated. With LCI techniques, it has been shown that by using a Mirau objective, the transmittance spectra of single absorbing layers can be locally measured from OCT data [17]. We then later showed using a Linnik-based FF-OCT system that a similar processing of the interferometric signals associated with the calibration of the system allowed the reflectance spectra of surfaces to be obtained with a good spectral resolution [18]. The advantage of this system is that the spectral information over the whole field of view and for each wavelength in the illumination spectrum is recorded at the same time. The acquisition time is limited by the number of sampled and averaged images over the optical axis, making this technique a convenient tool for local spectral measurements.

In the present work, the technique has been improved to enable the measurement of buried structures without the need to take into account the spectral influence of the other material in the layer. The area required to extract the interference signal is 3x3 or 5x5 pixels, corresponding

to an area of $0.34 \times 0.34 \mu\text{m}^2$ ($0.12 \mu\text{m}^2$) or $0.57 \times 0.57 \mu\text{m}^2$ ($0.32 \mu\text{m}^2$). Because the radius of the Airy disk is theoretically equal to $0.61\lambda/NA = 0.72\mu\text{m}$ for a wavelength of $0.65 \mu\text{m}$ and NA of 0.55, the measurement is therefore performed over an area of only $1.63 \mu\text{m}^2$, defining the lateral resolution of the measurement. The lateral resolution slightly decreases for depth-resolved measurements because of the necessity of working with a smaller effective numerical aperture. In this work, thin and transparent samples have been chosen to be investigated. Beginning with such samples is the simplest way to validate the technique by means of comparison with the results from simulation software. The studying of a thick, absorbing and scattering medium would make it more difficult to identify the different problems that may be involved in the spectral analysis over depth, both from an experimental and simulation point of view, and will be the subject of the next step in the work.

2. Theoretical background

2.1. Interferometric signal for a transparent layer

Let us consider a transparent layer on a substrate (Fig. 1). The layer is characterized by its thickness e and its complex refractive index $n = \eta + j\kappa$. We denote by $S(\lambda)$ the intensity of the source as a function of the wavelength λ , θ_{\min} and θ_{\max} are the extreme angles of illumination, $k = 2\pi/\lambda$ is the wavenumber, ϕ_1 and ϕ_2 are the phase shifts introduced by the reflection on both interfaces, and θ' is the refraction angle which is given by $\arcsin(n^{-1} \sin(\theta))$ for the top layer in air. R_{ref} , R_{s_1} , R_{s_2} and T_{s_1} are respectively the intensity reflection coefficients of the reference mirror, the front and rear interfaces and the intensity transmission coefficient of the surface.

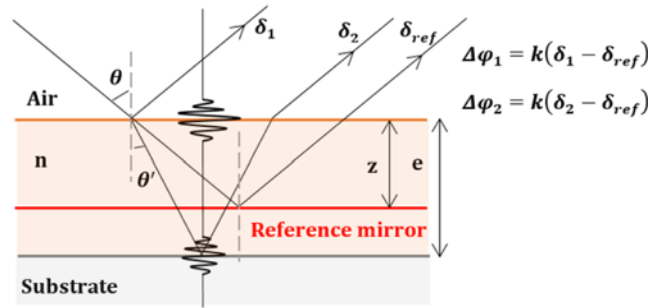


Fig. 1. Schematic representation of the phase shifts and the interferometric signal along the Z-axis in a transparent layer. Interferograms from the surface and the rear interface are shown.

After propagation through the interferometer, the intensity obtained is expressed as (the constant terms are suppressed):

$$I(z) \propto \int_{\theta_{\min}}^{\theta_{\max}} \int_0^{+\infty} \frac{1}{2} S(\lambda) \sqrt{R_{ref}(\lambda)} \left[\sqrt{R_{s_1}(\lambda)} \cos(\Delta\varphi_1(\lambda, z, \theta)) + \sqrt{R_{s_2}(\lambda)} T_{s_1}(\lambda) \exp(-2k\kappa) \cos(\Delta\varphi_2(\lambda, z, \theta)) \right] d\theta d\lambda \quad (1)$$

Where $\Delta\varphi_1(\lambda, z, \theta) = 2kz \cos(\theta) + \phi_1$ is the phase shift between the reference beam and the beam reflected by the surface, and $\Delta\varphi_2(\lambda, z, \theta) = 2k(z \cos(\theta) - e\eta \cos(\theta')) + \phi_2$ is the phase shift between the reference beam and the light reflected by the second interface.

2.2. Spectral analysis of the interferometric signal

Since the Fourier transform of the interference signal allows the recovery of the spectral properties of the structure at the origin of the interferogram as well as those of the entire optical system, it is necessary to process only the signal coming from the rear side of the layer. If $SpecResp_{cam}$ is the spectral response of the camera and T_{sys} is the spectral transmission of the system, then the following equation gives the relationship between the spectral transfer function of the system and the interference fringes from the second interface:

$$\left| FT \{ I(\delta) \}_{s_2} \right| = \frac{1}{2} S(\sigma) \sqrt{R_{ref}(\sigma)} \sqrt{R_{s_2}(\sigma)} (1 - R_{s_1}(\sigma)) \exp(-4\pi\sigma\epsilon\kappa) \cdot SpecResp_{cam} \cdot T_{sys} \quad (2)$$

Where $\sigma = 1/\lambda$ is the wavenumber, and $\delta = 2z$ is the optical path difference. Hence, it is necessary to know both the reflectance of the surface as well as the spectral signature of the system to determine the desired spectrum. This is achieved by carrying out three spectral measurements, with one of them on a sample of known reflectance, the so called “calibration sample”. By taking care to perform these three measurements in the same experimental conditions and at the same point in the image, the reflectance spectrum of the buried interface is then given by:

$$R_{s_2}(\sigma) = \frac{\left| FT \{ I(\delta) \}_{s_2} \right|^2}{\left| FT \{ I(\delta) \}_{cal} \right|^2} \frac{R_{cal}(\sigma)}{(1 - R_{s_1}(\sigma))^2} \quad (3)$$

With R_{cal} the reflectance of the calibration sample and $FT \{ I(\delta) \}_{cal}$ the Fourier transform applied to the calibration signal. The absorption effects occurring during the propagation through the layer are included in the term R_{s_2} . As regards the spectral resolution achievable, several factors need to be considered. In general, there is always a trade-off between the spatial and spectral resolution. An increase in the spectral resolution is normally achieved by processing the signal with a very high length (i.e. containing a high number of measurement points). In our case, before the processing, the interferograms are selected using an apodisation window which is centered on the maximum amplitude of the interferogram along the Z axis. These interferograms are usually spread over a small distance of the order of 3 μm due to the use of a broad white light spectrum. To obtain a high spectral resolution, while larger windows would be more suitable, this would lead to the inclusion of too much noise in the calculation from the parts of the signal outside of the 3 μm wide interferogram where the signal to noise ratio is very low. Consequently the window size is generally the same as that of the interferogram. An increase in the spectral resolution would therefore result from using a narrower spectrum (interferogram larger over Z), which would decrease the measurable wavelength range and decrease the axial resolution. In our case, the ability to measure the reflectance spectrum of a buried interface regardless of the covering layer relies on the ability to correctly separate the interferograms along the Z-axis. We have therefore chosen to favor a good axial resolution, defined by the Full Width at Half Maximum (FWHM) of the interferogram envelope. In order to still maintain a good spectral resolution, we have nevertheless chosen to use truncated signals with the highest length allowed by the separation of the interferograms. Then, to reduce the temporal noise, N consecutive images (N is set according to the quality and the desired acquisition time) are averaged at each piezoelectric displacement step ($\delta z = 50\text{nm}$) [19]. The spectral resolution then depends on the thickness of the layer or the random distribution of structures along the depth for more complicated samples. For the sample investigated here, the width of the window is equal to 6.5 μm (130 points) and

the spectral resolution, which is defined as the FWHM of the Fourier transform of the window, is equal to 30 nm at a wavelength of 650 nm in the case of a Hamming window. Before being Fourier transformed, each signal is increased in size to 4096 points using a zero-padding loop. This last operation enables a higher spectral sensitivity to be obtained $\delta\sigma = (2\delta zN)^{-1} = 24 \text{ cm}^{-1}$ ($\delta\lambda = \delta\sigma \cdot \lambda^2 = 1 \text{ nm}$ at $\lambda = 650 \text{ nm}$).

If the processing is applied to the whole interferometric signal, including both interferograms, then the reflectance spectrum of the transparent sample is obtained. Some examples of total reflectance spectrum measurements are also presented in which the accessible spectral resolution is even better due to the processing of signals of higher length.

3. Experimental setups

The proposed spectroscopic method was tested with two kinds of interferometric systems using the Mirau and Linnik configurations. The first one is a lab built Mirau-based microscope consisting of tube-mounted optical and optomechanical components and white light LED illumination (Fig. 2(a)). While easy to align, this setup does not allow control of the illumination aperture and some of the incident light is blocked by the reference mirror (blue rays). The second system (Fig. 2(b)) consists of a modified Leitz-Linnik interference microscope with two identical x50 objectives (NA = 0.85) and a halogen lamp illumination source. In this case, an aperture diaphragm does allow the control of the illumination angle. The samples are investigated over depth in both systems by changing the distance between the objective and the sample surface. Z-scanning is achieved using a piezoelectric table (PIFOC, PI) which is either directly mounted on the Mirau objective, or positioned under the sample. For both setups, the piezo actuator is controlled in a closed loop with a capacitive position sensor, having a position sensitivity of 1 nm. The signal acquisition is performed with a Photonfocus monochrome camera having 1024x1024 pixels and a Giga ethernet connection. In order to respect the Nyquist-Shannon sampling theorem, the displacement step is adjusted to 50 nm, which ensures a good sampling of the interferometric signal with a spatial frequency several times above the Nyquist frequency. System control and post processing are performed using a program developed in LabVIEW 2014 and the ImaQ vision module.

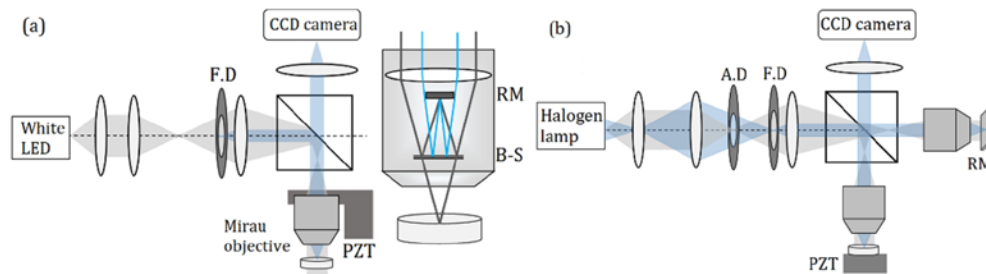


Fig. 2. Schematic representation of the experimental microscopes. (a) Mirau-based interference microscope and (b) Linnik-based interference microscope. A.D, aperture diaphragm; F.D, field diaphragm; RM, reference mirror; B-S, beamsplitter; PZT, piezoelectric device.

4. Results

The experimental measurements were performed on a transparent layer of PMMA (polymethyl methacrylate) deposited on a silicon substrate. Due to the properties of the polymer and the spin coating deposition method, the layer is quite inhomogeneous, leading to a variation in thickness from 2.5 μm to 4 μm over the field of view. In order to check the results obtained over depth, a simulation program based on the electromagnetic matrix methods for stratified media (S-matrix [20]) and inspired from [21] has been used. In this section, only the results obtained with

the Mirau-based interference microscope are shown, the experiments made in Linnik configuration leading to similar results.

4.1. Comparison between experimental and theoretical results at medium NA

In this section, the experimental results obtained with the Mirau microscope are compared to those obtained using the S-matrix program. The parameters required by the program are the complex refractive index of the materials, the thickness of the transparent layer, and the illumination aperture. Although the given numerical aperture for the Mirau objective is equal to 0.55, it was found from the comparison between experiments and simulations that the actual aperture of the system is lower (0.32). The thickness of the film was measured to be $3.33 \mu\text{m}$ in the area where the spectral measurements were performed by looking at the optical path difference between the signals coming from the rear and front sides of the layer [22]. The refractive index of the materials was taken from data given in the literature [23–26]. In the simulation, the reflectance spectrum for unpolarised light was then obtained from the average between the reflectance in intensity calculated for the s (TE) and p (TM) polarization.

The measurement of the reflectance spectrum was repeated 50 times at different points on the sample where the thickness was checked to be the same. The mean value of these 50 measurements, as well as the standard deviation, defined by Eq. (4), are plotted in Fig. 3.

$$\sigma(\lambda) = \sqrt{\frac{1}{N} \sum_{i=1}^N (R_i(\lambda) - \bar{R}(\lambda))^2} \quad (4)$$

With $N = 50$, the number of reflectance measurements, $R_i(\lambda)$ the reflectance calculated at the wavelength λ , and $\bar{R}(\lambda)$, the average reflectance which is given by:

$$\bar{R}(\lambda) = \frac{1}{N} \sum_{i=1}^N R_i(\lambda). \quad (5)$$

Then, the reflectance spectra are plotted as $\bar{R}(\lambda) \pm \sigma(\lambda)$.

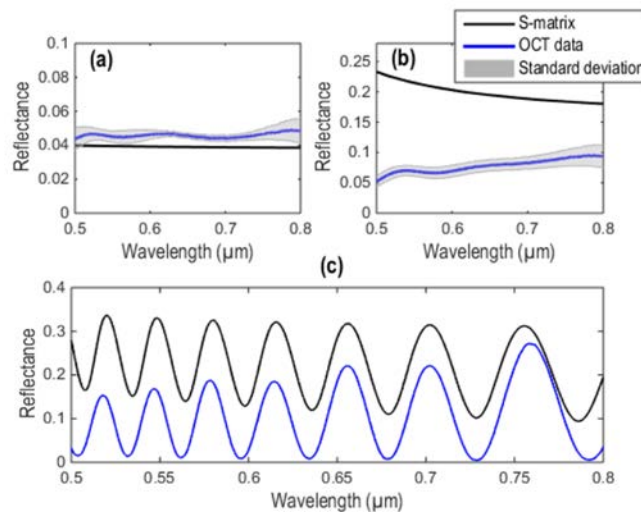


Fig. 3. Results of reflectance spectra for (a) Air-PMMA surface. (b) PMMA-silicon interface. (c) Combined layer (total reflectance spectrum) at a NA of 0.32. The black and blue curves are respectively obtained from the S-matrix program and from the OCT experimental data. The grey area shows the standard deviation of the measurements at each wavelength defined by Eq. (4).

It can be noticed that while the experimental and theoretical spectra for the air-PMMA surface are in good agreement (Fig. 3(a)), those for the buried PMMA-silicon interface are quite different (Fig. 3(b)). While the results for the total layer are similar in form, they nonetheless include differences (Fig. 3(c)). Since the thickness as well as the optical index of the layer are related to the modulation of the spectrum [27,28], the slight difference in the period of the latter can be explained by their values for dispersion used in the program which may be slightly different from the real ones (Fig. 3(c)). The value of the obstruction angle θ_{\min} (for the Mirau objective) and the spectrum distortion occurring after the processing (see section B.2) could also be a source of explanation. However, the observation of the surface reflectance spectrum (air-PMMA surface) shows that this experimental result matches with the expected one (Fig. 3(a)). Because the spectrum of the surface is consistent, we deduce that the error comes from the second signal.

4.2. Identification of error sources for the depth-resolved spectral analysis

4.2.1. Simulations: total and depth-resolved reflectance measurements for different illumination apertures

In order to understand why the measurement errors might come from the second signal, the results obtained with the S-matrix method were compared with those from a simulation program developed in-house in LabView (WILIS) [29] for determining the interference signal expected in different situations and in particular in a multilayer. The WILIS program allows the instantaneous observation of the influence of various parameters (spectrum shape, source temperature with selection of the black body source, numerical aperture, thickness and refractive index of each layer) on the interference signal resulting from a standard white light interference configuration (Fig. 2). The optical index can be determined using either Cauchy's or Sellmeier's law, loaded from experimental tables or adjusted at a constant value. Then the reflectance of each interface is given by the Fresnel coefficients for s and p polarizations. The sample of the thin layer of PMMA deposited on silicon was then simulated. The parameters (thickness, optical index, NA) are of course identical for both programs. The angle of incidence varies from θ_{\min} (obscuring angle in the Mirau configuration) to θ_{\max} ($\arcsin(\text{NA})$). To come as close as possible to the experimental effective spectrum (i.e. the product of the source spectrum with the camera spectral response) the spectrum shape defined by Eq. (6) is chosen in the program to have a center wavelength of 650 nm and a width of 150 nm (Fig. 4).

$$S(\sigma) = \frac{I_0}{1 + 4 \frac{(\sigma - \sigma_0)^2}{\Delta\sigma^2}} \text{ with } \sigma = \frac{1}{\lambda} \text{ and } \Delta\sigma = \frac{\Delta\lambda}{\lambda_0^2} \quad (6)$$

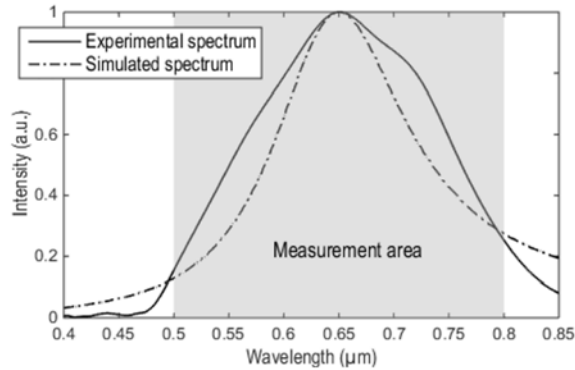


Fig. 4. Experimental and simulated source spectra. The spectrum in the solid line is obtained from the FT of one interferogram for a simple silicon substrate. The spectrum in the dashed line is obtained from Eq. (6).

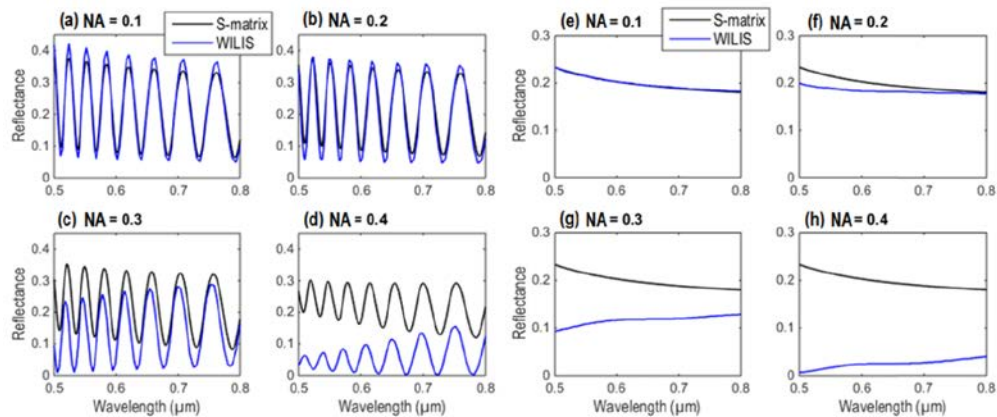


Fig. 5. Effect of the numerical aperture on both the total reflectance spectrum (a), (b), (c), (d) and the buried PMMA-silicon interface reflectance spectrum (e), (f), (g), (h), and comparison between the results obtained using an electromagnetic program (S-matrix; black curves) and from the processing of interference fringes (blue curves).

It becomes obvious from observing the results in Fig. 5 that the numerical aperture leads to errors in the spectral analysis. For very small NA (< 0.2), there is a little difference in the amplitude between the two total reflectance spectra: this could be explained by the multiple reflections occurring between the front and rear sides of the layer that are taken into account in the S-matrix simulation but not in the WILIS program. Even for surface measurements, it has been shown that the numerical aperture leads to errors due to the increase in the interfringe distance [30–32] (the increase in the interfringe is the same for both interferograms at a given angle of incidence), introducing a spectrum dilatation [18]. The correction proposed by Morin et al. [33] has been applied to overcome this problem of spectrum distortion. Indeed, the aperture correction factor β , defined by the ratio between the measured central wavelength and the real illumination central wavelength, is automatically calculated in order to obtain each spectrum centered on the real effective wavelength. According to the previous results, the numerical aperture is the main factor causing errors in the measurements. In the following, two effects of the NA on the fringes are discussed, and then the experimental results are compared with those obtained with the WILIS program.

4.2.2 The NA and its influence on the second interference signal

The first effect is related to the refraction phenomenon taking place at the air-PMMA surface. When the layer is illuminated by a sum of convergent rays having multiple angles of incidence θ , the different beams passing through the surface will be refracted at different angles θ' and will thereby interfere constructively at different positions of the sample, in accordance with the relationship:

$$z(\lambda, \theta) = \frac{m\lambda}{2\cos(\theta)} + en\frac{\cos(\theta')}{\cos(\theta)}; \quad m \in \mathbb{Z} \quad (7)$$

If the function $z(\lambda, \theta)$ is differentiated with respect to θ , it is then possible to observe the variation of position of the signal maxima (white fringe) as a function of both θ and λ (Fig. 6). In these simulations, the shift of the central fringe due to the phase change on reflection and which increases with the NA is not taken into account. Indeed, even for metallic materials presenting a high phase change on reflection, the central fringe shift remains relatively low [34].

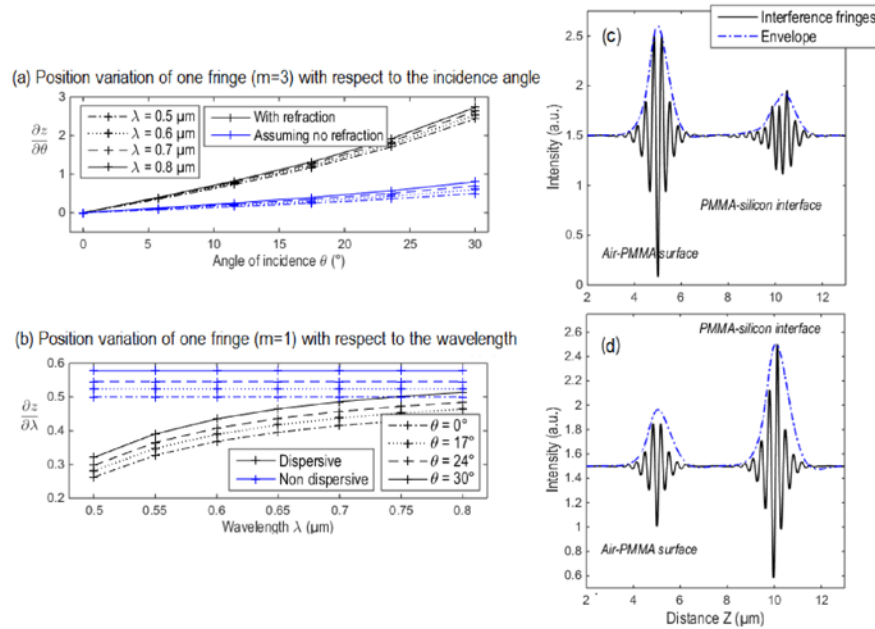


Fig. 6. (a) Derivative of z with respect to θ : variation of position of the third white fringe ($m = 3$) as a function of the angle of incidence for different wavelengths. The result is compared to that obtained by assuming no refraction, i.e. $\theta' = \theta$ (blue curves). The sample is assumed to be non-dispersive with a constant refractive index of 1.49. (b) Derivative of z with respect to λ : variation of position of the white fringe ($m = 1$) as a function of the wavelength for different angles of incidence. The result is compared to that obtained by assuming no dispersion (blue curves). (c)-(d) Simulated fringes with a NA of 0.5 with the refraction taken into account (c), and assuming no refraction, i.e. $\theta' = \theta$ (d). In each case, the signals are normalized with respect to the maximum intensity.

The graphs in Fig. 6(a) demonstrate that, due to refraction at the top of the sample, the position of the signal maximum (white fringe) depends strongly on the angle of incidence. In addition, the evolution of this position is non linear and becomes greater with the increase in the angle, resulting in a greater attenuation of the signal amplitude (Fig. 6(c)). By simulating the interferometric signal coming from the transparent sample in each case (with and without

refraction), the effect of the refraction on the amplitude of the second interferogram can be clearly observed (Figs. 6(c) and 6(d)).

It can be noted that the variation is even more significant when the layer is highly dispersive because of the dependence of the angle of refraction θ' on the wavelength (Fig. 6(b)). In the case of a non-dispersive layer the variation of position with respect to the wavelength is identical for any wavelength for a given angle of incidence. As soon as the layer is very slightly dispersive, which is the case for the PMMA, having a quasi constant optical index in the range of 0.5-0.8 μm , the position variation will then vary with the wavelength for the same incidence. Due to the decrease in amplitude, the spectrum calculated from the 2nd signal will be biased, resulting then in an incorrect measurement.

The second effect relates to the shift of the coherence and focal planes during the sample measurement over depth. This shift appears as soon as the sample refractive index differs from that of the immersion medium (air). Because of this refractive index mismatch the two planes move in opposite directions [35]; when the sample is elevated by a distance z , the focal plane moves by a distance nz , while the coherence plane is shifted by a distance $-z/n$. As long as the position of the two planes matches, the interferometric signal amplitude is maximal, but, once the planes move differently, the signal amplitude decreases until it becomes equal to zero when the two gates no longer overlap (defining then the maximum imaging depth). To observe whether the shift of the planes has a significant influence on the measurement, we simulated the interferometric signals for different NA by taking into account the shift in the planes. Following the calculations made in [36], let Δf_n and Δc_n be the FWHM of the focal and coherence gates respectively. The distance between the centers of both gates is Δg . The term Δc_n generally defines the axial resolution of the system and is related to both the center wavelength and the bandwidth of the source spectrum [37,38].

The shape of the coherence gate, or spatial coherence envelope (SCE), is given in the form of a cardinal sine function, due to the depth of field [39].

$$SCE(Z) = \left(\frac{\sin(Z)}{Z} \right)^2, \quad Z = \frac{\pi NA^2 z}{2\lambda_0 n} \quad (8)$$

With the layer having a thickness e of 3.33 μm , the sample has to be elevated by a distance ne to match the coherence plane with the second interface. Then Δg is given by $e(n^2 - 1)$. The graphs in Figs. 7(a) and 7(b) show the effect of the shift between the focal and coherence gates on the interference signal for an NA of 0.4. This value of NA is chosen in order to clearly reveal the shifting effect. For a thickness of 3.33 μm and a refractive index of 1.49, Δg is equal to 4.06 μm . The reflectance spectrum of the PMMA-silicon interface was then measured for each case. The only difference that can be observed is an amplitude offset (Fig. 7(c)). For the NA used in our system, the error induced by the shift is not very significant and can be ignored. However, to entirely suppress this shifting effect, increasing the depth of field (\sim FWHM of the cardinal sine function) by reducing the NA is one of the simplest solutions.

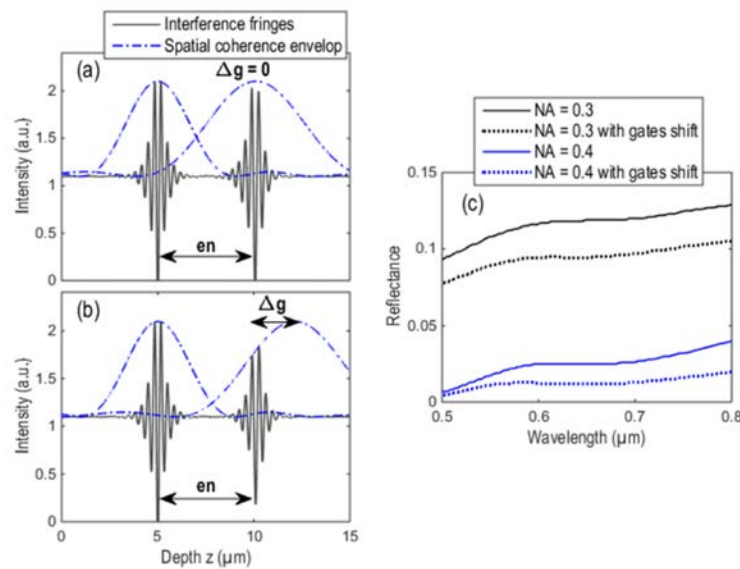


Fig. 7. Influence of the spatial coherence on the interference signal when a dispersion mismatch occurs. (a) The coherence plane is assumed to match with the focal plane. (b) The planes are separated by a distance of $\Delta g = 4.06 \mu\text{m}$. The NA is set to 0.4. (c) Modification of the PMMA-silicon interface reflectance spectrum.

When working in the Linnik configuration, a better way is to perform dynamic focusing; that is, to move and adjust the coherence and focal gates independently of each other [40]. In this way, the two planes always match and the amplitude of the second interferogram remains unchanged. However, during the image stack acquisition, two motorized stages are required for moving both planes simultaneously, which was not possible with the present optical arrangement.

4.2.3 Comparison of spectra between experimental OCT data and WILIS simulation at medium NA

The results obtained in sections 4.2.1 and 4.2.2 have shown that the experimental measurements contained errors related to the NA used. To ensure that the illumination aperture is the main source of error in the depth-resolved spectroscopic analysis, the experimental measurements made at medium aperture were compared to those obtained with the WILIS program and checked to be the same. For the simulations, the effects resulting from the illumination aperture presented above were taken into account. The total reflectance spectrum of the sample as well as the depth reflectance spectrum were simulated for several values of the NA. This showed that the results match almost perfectly for an effective NA of 0.32. The standard deviation (defined by the grey area) and the average spectrum were still both calculated from 50 measurement points (Fig. 8(a)). It can be observed that for the spectrum measured from the buried interface, the simulation is included in the margin of error of the measurement, resulting in an almost perfect match. For the total reflectance spectrum (Fig. 8(b)), no spatial averaging is performed, the blue curve being only obtained from one area (5x5 pixel binning). The experimental and simulation results are very close to each other; the slight difference of spectrum modulation being attributed as previously to the thickness, refractive index, and obstruction angle used in the simulation program. Measurement of the PMMA refractive index was also performed using a Jobin-Yvon ellipsometer but did not lead to usable results due to the non-flatness and excessive thickness of the layer resulting in too fine oscillations that could not be resolved. The good match between these results reveals that the NA is indeed the main

source of error in the depth-resolved spectral analysis, and then underlines the interest of working with a smaller illumination aperture.

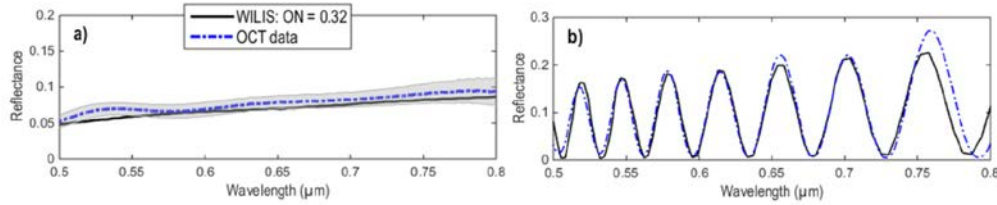


Fig. 8. a) PMMA-silicon interface reflectance spectrum. b) Total reflectance spectrum. The black and blue curves are respectively obtained from the WILIS program and from the measured OCT data.

4.3. Measurements made with small numerical aperture (< 0.2)

When working with a NA higher than 0.2, several problems occur in the spectral analysis of buried interfaces and structures according to the previous simulations and experiments. The best solution then is to work at normal incidence by reducing the effective NA. In this case, the different incident beams reflected by the buried interface no longer mix with each other, so preventing the amplitude loss of the second signal. In addition, reducing the effective NA results in an increase in the depth of field of the system and an overcoming of the problem of the shift in coherence-focal planes [41]. But, working with a small NA (< 0.2) leads to two disadvantages. Firstly, a large amount of energy is lost during the light propagation through the illumination arm, which can be an important issue when the sample is very transparent or highly absorbing. Secondly, the spatial resolution is inevitably worse. This point is discussed further in section 4.4. In this section, the measurements were only carried out with the Leitz-Linnik interferometric system due to the need to decrease the effective NA. Indeed, the blocking of the central light rays due to the reference mirror in the Mirau configuration prevents the working at near-to normal incidence. The effective NA of the Linnik system was reduced as much as possible by closing the aperture diaphragm and was determined to be approximately at a value of 0.1 by comparison to simulated spectra. The illumination source being a halogen lamp, the measurements were performed in the 550-1000 nm wavelength range. The experimental results are plotted in Figs. 9(a) and 9(b) and compared with those obtained using the S-matrix simulation program. A very good match can be observed between the experimental and simulation results in both cases. The greater difference in the 0.5-0.55 μm range, as well as the standard deviation increase, is related to the fact that the effective spectrum is no longer well defined in this range (the signal to noise ratio is low as shown in Fig. 9(c)). Moving out of the 0.55-1 μm spectral band, the useful signal amplitude decreases to the point where the noise begins to have a significant influence, so rendering the measurements invalid.

By performing 100 successive measurements of the spectrum, we established that the measurement can be considered reliable for a signal to noise ratio (SNR) greater than 25 dB (Fig. 9(c)). The SNR data is obtained from the following equation:

$$SNR(dB) = 20 \log_{10} \left(\frac{A_{signal}}{\sigma} \right) \quad (9)$$

with A_{signal} the average amplitude of the spectrum and σ the standard deviation from 100 measurements.

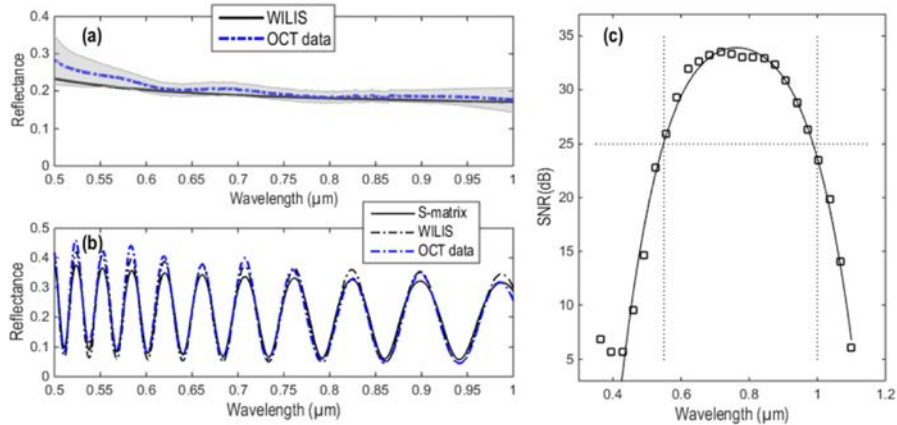


Fig. 9. (a)-(b) Comparison between experimental (blue curves) and theoretical spectra (black curves) for depth-resolved and total reflectance spectrum measurements for very low NA (~ 0.1). (a) PMMA-silicon interface reflectance spectrum. (b) Total reflectance spectrum. For simulations, the NA is adjusted to 0.1. (c) Signal to noise ratio measured over the spectral band considered. The two vertical dotted lines define the domain where the measurement is reliable.

According to the theory developed, the total reflectance spectrum should better match the results obtained with the WILIS program. Indeed, the S-matrix simulation takes into account the light reflected after the multiple reflections between the front and rear sides of the layer. In the case of the experimental measurements in which only the two first interferograms are processed, the light due to the multiple reflections is ignored since it is attenuated by the limited depth of field and coherence length. It is possible to confirm this assumption by calculating the quadratic error in each case, resulting in 0.0258 for the S-matrix and 0.0208 for WILIS results. While these results are consistent with the theory, they are not really relevant due to the small difference between these values. The angle of incidence varying from 0 to $\arcsin(0.1)$, the possible errors related to both the obstruction angle and the aperture correction factor β are eliminated and we note, in both cases, that the slight difference in the period has disappeared.

4.4. Spatial resolutions of the measurements

The local spectral measurements are spatially resolved in the transverse and axial directions. The values of these resolutions are important because they refer to the smallest sized structure that is possible to spectrally characterize independently from the rest of the sample. If two single structures are closer than the distance set by the spatial resolutions, it will be difficult to separate their spectral response. For the next results, we consider the parameters of the Leitz-Linnik interferometer using an objective NA of 0.85 and a spectral bandwidth of 280 nm with a central wavelength of 800 nm.

4.4.1. Lateral resolution

As in any imaging device, the lateral resolution is usually given by the FWHM of the point spread function (PSF) of the system which is, in the case of a diffraction-limited optical system, the Airy function (Eq. (10)) [42]:

$$h(u) = \left[\frac{2J_1(u)}{u} \right]^2, \quad u = \frac{2\pi}{\lambda} r NA \quad (10)$$

Where J_1 depicts the Bessel function of the first kind and first order. The lateral resolution is then approximately defined by the radius of this function which is $\Delta x = 0.61\lambda/NA$ for incoherent illumination. When closing the aperture diaphragm, the degree of spatial coherence

of the illumination increases and involves then a decrease in the lateral resolution. Several criteria and methods have been introduced to estimate the resolution of an optical system. In the reference [43], it is defined from the imaging of two pinholes of equal brightness. It is shown that, assuming the Rayleigh criterion, if m denotes the ratio between the numerical apertures of the illumination (defined by the diaphragm) and the objective, it follows that the resolution is given by $\Delta x = L(m)\lambda/NA$ where $L(m)$ varies between 0.84 and 0.56 as a function of m . The lateral resolution can also be experimentally found by simply recording the intensity profile along a perfect edge and measuring the 10-90% rise distance [44,45] (the response through the microscope being the convolution of this step with the PSF). The technique finally used was based on the modulation transfer function (MTF) [46] which consists in measuring the intensity profile of a periodic grid and determining the spatial cut-off frequency (inverse of the resolution). A grid standard from SiMetricS consisting of multiple periodic patterns with varying periods was used. In this case, increasing the degree of spatial coherence of the illumination involves both a lower cut-off frequency and a better contrast for the smaller spatial frequencies. Theoretically (meaning aberration free), when moving from incoherent to almost coherent illumination (point source), the lateral resolution decreases from $\lambda/2NA$ to λ/NA [47]. This loss in resolution is checked by measuring the contrast of the intensity profile as a function of the spatial frequency. The results obtained with two extreme positions of the aperture diaphragm are plotted in Fig. 10(a). Here, the contrast transfer functions (CTFs) are plotted because the contrast measurement is made on a square grid. The MTF and CTF are quite similar and have the same cut-off frequency. When the diaphragm is totally open a cut-off frequency of 2 lines/ μm is obtained, resulting in a lateral resolution of 0.5 μm that is slightly larger than the theoretical value of 0.47 μm . From Fig. 10(a), it can be observed that the new lateral resolution after closing the diaphragm is 0.84 μm , which is well below the value of 0.94 μm calculated from λ/NA , meaning that the source can still not be considered as a point source. The necessity of working at small effective NA leads then to a lateral resolution loss of about 0.3 μm .

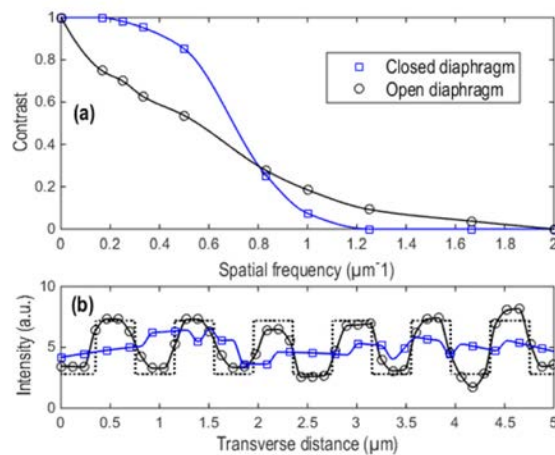


Fig. 10. (a) CTFs (Contrast Transfer Function) of the Leitz-Linnik setup for two positions of the aperture diaphragm. (b) Intensity profile of the 0.8 μm period grating obtained in the open (black line) and closed (blue line) positions of the diaphragm. The square curve in the dotted line represents the theoretical results.

4.4.2. Axial resolution

In the general case, the fringes visibility is adjusted by both the temporal and the spatial coherence of the system, in such a way that the term for the visibility V is given by [48]:

$$V = V_0 |\mu| |\gamma| \quad (11)$$

Where μ and γ are respectively the degree of spatial and temporal coherence of the source and V_0 is a constant depending on the intensity. The temporal coherence is proportional to the coherence length of the source while the spatial coherence depends on the NA of the objective and the spatial extent of the source. Consequently, depending on the properties of the system, the axial resolution, which is defined as the FWHM of the visibility will be mainly governed by either the coherence length or by the numerical aperture. The resolution can be expressed as follows in each case:

$$\Delta z_{temp} = \frac{2 \ln 2}{n\pi} \frac{\lambda_0^2}{\Delta \lambda}; \quad \Delta z_{spat} = \frac{7.6 \lambda_0}{\pi NA_{eff}^2} \quad (12)$$

Where each term corresponds to the FWHM of the functions $|\mu|$ and $|\gamma|$, and NA_{eff}^2 is the effective numerical aperture, depending on both the objective and the illumination numerical apertures. Closing the aperture diaphragm mainly results in only Δz_{spat} being highly degraded. The influence of each term, as well as the resulting theoretical axial resolution are plotted as a function of the effective NA in Fig. 11(a). The central wavelength is adjusted to 0.8 μm and two bandwidths are considered: 280 nm corresponding to the source used and 55 nm. In the cases where the temporal and spatial coherence have a similar influence, decreasing the illumination numerical aperture is significant, resulting in a decrease in the axial resolution (blue curve). In the case of the Leitz-Linnik (black curve), the effect of the temporal coherence is so predominant compared to the spatial effect, that the axial resolution remains almost constant whatever the effective NA. It follows that the axial resolution should be equal to approximately 1 μm in both illumination cases (Figs. 11(b) and 11(c)).

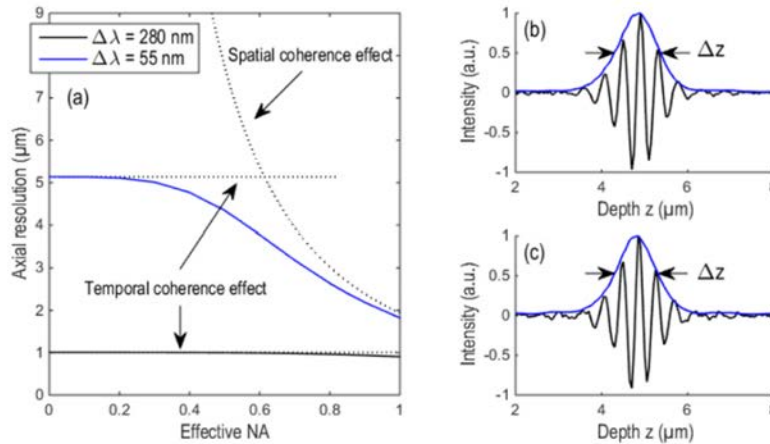


Fig. 11. (a) Theoretical axial resolution as a function of the effective NA for two source bandwidths. The illumination spectrum is centered at 800 nm. (b)-(c) Experimental axial resolution obtained for two extreme aperture positions of the diaphragm. (b) Fully open. (c) Closed as much as possible. The interferograms are obtained from a silicon substrate.

The axial resolutions were measured using the interferogram to be 1.05 μm and 1.08 μm for the respectively cases of (b) and (c), very slightly larger than the predicted values (0.95 μm and 1.01 μm) but still in good agreement with the theory.

5. Conclusion and perspective

A new application of FF-OCT for depth resolved reflectance spectra measurement has been presented. These first results have highlighted the need for performing a good calibration of the system, and the necessity of using small angles of incidence. Local reflectance spectra of a buried interface have been obtained on a transparent sample of PMMA deposited on silicon with a spectral resolution of 30 nm and have been validated by comparison with the results of simulation. Whatever the spectral band investigated and the size of the field of view, all the information is recorded at the same time, resulting in an acquisition time that is only limited by the number of sampling and averaging images along the optical axis. The spatial and spectral resolution are also independent from the acquisition time, the former being related to the properties of the optical system itself, and the latter being set by the spatial distribution of the structures along the depth into the sample. Spatial resolutions of 0.84 μm in the transverse direction and 1 μm in the axial direction have been demonstrated in spite of the need for increasing the degree of spatial coherence of the illumination. For the time being, only simple samples have been investigated where the dispersion remains relatively low and the absorption and the scattering phenomena can be ignored. Of course, in many samples, these mechanisms can have a significant influence. The combination of scattering and absorption phenomena, together with the necessity for working at small NA (< 0.2) would result in a significant loss in energy during the light propagation through the interferometer, thus requiring highly optimized illumination. Further work will concern the study and measurement of such samples. The first step will be to use immersion objectives to compensate the dispersion mismatch occurring between the two interferometer arms. Then, the decrease in the signal amplitude due to the fringe spreading should be avoided.

Acknowledgments

The authors would like to acknowledge the financial support of this work from the University of Strasbourg and INSA Strasbourg. The authors also wish to thank Stéphane Roques and the staff from the C³FAB platform for the sample preparation.